

The widest H α survey of accreting protoplanets around nearby transition disks \star

A. Zurlo^{1,2}, G. Cugno³, M. Montesinos^{4,5,6}, S. Perez⁷, H. Canovas⁸, S. Casassus⁹, V. Christiaens¹⁰, L. Cieza¹, N. Huelamo¹¹

¹Núcleo de Astronomía, Facultad de Ingeniería y Ciencias, Universidad Diego Portales, Av. Ejercito 441, Santiago, Chile

²Escuela de Ingeniería Industrial, Facultad de Ingeniería y Ciencias, Universidad Diego Portales, Av. Ejercito 441, Santiago, Chile

³ETH Zürich, Institute for Particle Physics and Astrophysics, Wolfgang-Pauli-Str. 27, 8093 Zürich, Switzerland

⁴Núcleo Milenio de Formación Planetaria (NPF), Chile

⁵Instituto de Física y Astronomía, Universidad de Valparaíso, Valparaíso, Chile

⁶Chinese Academy of Sciences South America Center for Astronomy, National Astronomical Observatories, CAS, Beijing, China

⁷Universidad de Santiago de Chile, Av. Libertador Bernardo O'Higgins 3363, Estacion Central, Santiago, Chile

⁸European Space Astronomy Centre (ESA/ESAC), Operations Department, Villanueva de la Cañada, Madrid, Spain

⁹Departamento de Astronomía, Universidad de Chile, Casilla 36-D, Santiago, Chile

¹⁰School of Physics and Astronomy, Monash University, VIC 3800, Australia

¹¹Centro de Astrobiología (CSIC-INTA), ESAC, Camino bajo del Castillo s/n, E-28692 Villanueva de la Cañada, Madrid, Spain

Submitted 2019 October, 10 / Accepted 2019 December, 9

ABSTRACT

Context. The mechanisms of planet formation are still under debate. We know little about how planets form, even if more than 4000 exoplanets have been detected to date. Recent investigations target the cot of newly born planets: the protoplanetary disk. At the first stages of their life, exoplanets still accrete material from the gas-rich disk in which they are embedded. Transitional disks are indeed disks that show peculiarities, such as gaps, spiral arms, and rings, which can be connected to the presence of substellar companions.

Aims. To investigate what is responsible for these features, we selected all the known transitional disks in the solar neighborhood (<200 pc) that are visible from the southern hemisphere. We conducted a survey of 11 transitional disks (TDs) with the SPHERE instrument at the Very Large Telescope. This is the largest H α survey that has been conducted so far to look for protoplanets. The observations were performed with the H α filter of ZIMPOL in order to target protoplanets that are still in the accretion stage. All the selected targets are very young stars, less than 20 Myr, and show low extinction in the visible.

Methods. We reduced the ZIMPOL pupil stabilized data by applying the method of the angular spectral differential imaging (ASDI), which combines both techniques. The datacubes are composed of the Cnt_H α and the narrow band filter H α , which are taken simultaneously to permit the suppression of the speckle pattern. The principal component analysis (PCA) method was employed for the reduction of the data. For each dataset, we derived the 5σ contrast limit and converted it in upper limits on the accretion luminosity.

Results. We do not detect any new accreting substellar companions around the targeted transition disks down to an average contrast of 12 magnitudes at 0".2 from the central star. We have recovered the signal of the accreting M star companion around the star HD 142527. We have detected and resolved, for the first time in visible light, the quadruple system HD 98800. For every other system, we can exclude the presence of massive actively accreting companions, assuming that the accretion is not episodic and that the extinction is negligible. The mean accretion luminosity limit is $10^{-6} L_{\odot}$ at a separation of 0".2 from the host.

Key words. Instrumentation: high angular resolution, high contrast, Methods: data analysis, Techniques: imaging, Stars: AKSco, V4046Sgr, HD169142, HD98800B, HD97048, HD100546, HD142527, HD141569A, HD135344B, PDS66, HD100453, UXTauA

1. Introduction

Detecting forming protoplanets is the cornerstone to understanding planet formation (Fortney et al. 2008; Spiegel & Burrows 2012; Mordasini et al. 2017). Approximately $\sim 30\%$ of Herbig Ae/Be disks should host giant planets of ~ 0.1 to $10 M_{Jup}$ (Kama et al. 2015). Some Herbig stars host transitional disks (TDs), which are peculiar disks with cavities, gaps, and spiral structures that can be induced by the presence of a companion (e.g., Dodson-Robinson & Salyk 2011). Supporting this theory, hydrodynamical simulations predicted the presence of substellar companions around some observed TDs (e.g., Dong et al. 2016a).

Accreting giant planets are thought to develop a circumplanetary disk (CPD) as they interact with the circumstellar material (e.g., Miki 1982; Gressel et al. 2013; Perez et al. 2015). While a fraction of the mass flows through the CPD at midplane latitudes, a substantial amount of gas falls onto the surface of the CPD via meridional flows (Tanigawa et al. 2012; Morbidelli et al. 2014; Szulágyi et al. 2014). The vertical accretion flow happens at near free-fall speeds, thus shocking the CPD surface and heating the gas to thousands of kelvin. H α emission is thought to arise from the hot, shocked surface (Aoyama et al. 2018). Additionally, the intrinsic planet luminosity also contributes to heat up the circumplanetary environment, while enhancing the stellocentric accretion rate (Montesinos et al. 2015).

\star Based on observations collected at the European Southern Observatory (ESO), programs number 096.C-0267, 096.C-0248, 099.C-0453, 0100.C-0193, 0101.C-0461, 0102.C-0138.

Breakthroughs in $H\alpha$ high-contrast imaging, which is an indicator of accretion on compact bodies (Rigliaco et al. 2012; Tambovtseva et al. 2014; Zhu 2015b), have recently triggered intense interest. Notably, the first successful $H\alpha$ detection of a close stellar companion was found around the star HD142527 (Close et al. 2014), and was followed by the detection of an accreting protoplanet candidate around the transition disk LkCa15 (Sallum et al. 2015). The emission from the potential protoplanet is at the same location of the scattered light of the interior part of the disk (Thalmann et al. 2016), and it is hard to disentangle the two components. The presence of such a protoplanet is a subject of debate (see Mendigutía et al. 2018; Currie et al. 2019). The most evident case of an accreting protoplanet in a transition disk is PDS70b, where a clear detection in the near-infrared (NIR) has been recovered (Keppler et al. 2018; Müller et al. 2018; Christiaens et al. 2019; Mesa et al. 2019). Subsequently, Wagner et al. (2018) found $H\alpha$ emission coming from the location of the protoplanet, demonstrating that the object is currently actively accreting with a mass accretion rate of $\dot{M} = 10^{-8\pm 1} M_{\text{Jup}} \text{ yr}^{-1}$. Recently, a second accreting protoplanet around the same star was detected in $H\alpha$ emission with the multi-unit spectroscopic explorer (MUSE) instrument by Haffert et al. (2019). Finally, Cugno et al. (2019) published a first $H\alpha$ survey focusing on targets that are suspected of hosting forming companions; they were unable to find any new unknown accretion signals.

Imaging young (a few Myr old) disks in $H\alpha$ could potentially be sensitive to low-mass planets, even if they have moderate accretion rates ($\dot{M} > 10^{-5} M_{\text{Jup}} \text{ yr}^{-1}$; Close et al. 2014). These values were estimated by converting the accretion rate of a low-mass object to $H\alpha$ luminosity by using the T Tauri stars relation presented in Rigliaco et al. (2012) in order to predict the contrast in $H\alpha$, showing that observations are more favorable for planetary objects with respect to any other NIR observation (Fig. 5 of Close et al. 2014). This is the case even though the two recent papers by Thanathibodee et al. (2019) and Aoyama & Ikoma (2019) demonstrate that the $H\alpha$ emission from the planets comes from different mechanisms.

For this purpose, we selected all the known TDs that are closer than 200 pc and observable with the SPHERE planet finder at the Very Large Telescope (VLT, Chile). We found 11 targets, and for completeness we added three targets from the archive. The selected stars are young (age < 20 Myr), and all of them have very low extinction in the visible (a fraction of a magnitude). Our targets are young stars with disks that present spirals, cavities, or gaps, and even in some cases, in both gas and dust. Material ought to flow from the outer disk reservoir and cross the gap to replenish the material being accreted by these stars. Hydro simulations suggest that the most obvious gap crossing mechanism is through the protoplanet’s wake streams.

The outline of the paper is as follows. In Sec. 2, we describe our target selection and present the SPHERE $H\alpha$ observations of the systems; in Sec. 3, we describe the reduction methods applied and the results that we obtained in Sec. 4. We give the discussion and conclusions in Sec. 5.

2. Observations

2.1. Target selection

Our survey targets all the known TDs that are closer than 200 pc and observable from the VLT. Some of them had already been observed in a similar configuration of the instrument and for the same purpose. The data were already available in the archive. The individual target PDS 70, which was initially selected as

part of the sample before the discovery of the companions b and c (Keppler et al. 2018; Haffert et al. 2019), has been removed from this analysis, as it will be presented in a separate and future paper. The stars included in the sample are listed - together with their main properties - in Table 1.

The disks around MWC 758, HD 135344 B, HD 100546, AK Sco, and HD 100453 present spirals that can be induced by the presence of a companion. For MWC 758, Dong et al. (2015) predict the presence of a $\sim 10 M_{\text{Jup}}$ companion at 160 au, which could have shaped the disk. Then, Reggiani et al. (2018) present a companion candidate at 20 au, and their contrast curves rule out companions larger than $5 M_{\text{Jup}}$ beyond the spirals ($\sim 0''.6$), assuming hot-start models. For HD 135344 B, similarly, van der Marel et al. (2016) and Hammer et al. (2019), connect the presence of the spiral features of the disk with the dynamical interaction with companions. For HD 100546, protoplanet candidates were actually found: Quanz et al. (2015) confirm a candidate observed in different bands (L' and M'). A second candidate was found by Currie et al. (2015) using the Gemini Planet Imager (GPI, Macintosh et al. 2006) instrument. Recently, both Rameau et al. (2017) and Sissa et al. (2018) suggest that the candidates are more likely disk features. Mendigutía et al. (2017) found a bar-like structure in the polarized $H\alpha$ emission around the star. For AK Sco, Janson et al. (2016) found two spiral arms in scattered light, which can be induced by the presence of a companion. For the spiral structures around HD 100453, Dong et al. (2016b) prove, with dynamical simulations, that they are induced by the stellar object detected in NIR light at a projected distance of ~ 119 au. For the stars HD 142527 (Close et al. 2014) and HD 98800 BaBb (Furlan et al. 2007), for which accreting companions are found, we refer the reader to the dedicated Sections 4.1 and 4.2, respectively.

Some TDs present gaps and rings that can be carved by planets: around V4046 Sgr AB, rings are found at 14 au and 29 au (Rapson et al. 2015) as well as 40 au (Avenhaus et al. 2018). The disk around HD 169142 has a gap at 23 au (Honda et al. 2012) and in scattered light at 40 au (Pohl et al. 2017). Around this star, a protoplanet candidate was claimed by Reggiani et al. (2014) and Biller et al. (2014), even if this detection has since been disputed (Ligi et al. 2018). DoAr 44’s disk has a gap from 5 au to 32 au (Casassus et al. 2018); in scattered light it resembles a scaled down version of HD 142527 (Avenhaus et al. 2018). The presence of an inner warp in this disk may be caused by a planet (Casassus et al. 2018). The TD around HD 97048 has gaps at 34, 79, 140, and 179 au, and four rings (Ginski et al. 2016). Very recently, Pinte et al. (2019), presented the detection of a doppler kink in the gas flow of the disk. This Keplerian deviation can be explained by the presence of a planet that perturbs the gas flow (Perez et al. 2015). The kink is located exactly in one of the gaps, which is seen in both the ALMA continuum and in the scattered light images. For HD 141569 A, Perrot et al. (2016) found ringlets at 47 au, 64 au, and 93 au. The UX Tau A disk has an inner cavity at 56 au (Espaillat et al. 2007). PDS 66 has an inner cavity up to 15 au (Gräfe & Wolf 2013; Wolff et al. 2016).

2.2. Observations

This survey has been carried out with the instrument SPHERE (Beuzit et al. 2019). SPHERE is a planet finder at the ESO’s VLT that is equipped with an extreme adaptive optics system

Table 1: List of objects included in the sample with their main characteristics. The objects marked with * have been included for completeness, but they are a part of other observing programs. All the distances are taken from [Gaia Collaboration \(2018\)](#) apart, from the one of HD 98800B, which is from [van Leeuwen \(2007\)](#). References on the peculiarities of each disk are found in the main text.

Name	Sp. Type	d (pc)	Age (Myr)	Planet formation/presence indicators
MWC 758*	A8Ve	160	1.5 ^a	Spiral arms, possibly shaped by a $\sim 10 M_{Jup}$ companion at 160 au
HD 135344 B*	F8V	136	8 ^b	Possible planet induced spiral features
HD 142527*	F6III	157	5 ^c	Accreting stellar companion, inner warp, outer two-arms spirals disk
HD 100546	B9V	110	5 ^d	Spirals, protoplanet candidates, bar-like structure
HD 98800 B	K5	47	7–10 ^e	Gap from 2 to 5.9 au
AK Sco	Ae	141	10–20 ^f	Two spiral arms with extension of 13–40 au
V4046 Sgr AB	K5V	72	10–20 ^g	Rings at 14, 29, and 40 au
HD 169142	B5V	114	3–12 ^h	Gap at 23 and 40 au
DoAr 44	K3	146	7 ⁱ	Gap from 5 to 32 au, a rescaled version of HD 142527, inner warp
HD 97048	A0V	185	2–6 ^j	Gaps at 34, 79, 140 au, and 179 au and 4 rings
HD 141569 A	A0Ve	106	5 ^k	Ringlets at 47 au, 64 au, and 93 au
UX Tau A	K2Ve	140	1 ^l	Gap at 56 au
HD 100453	A9Ve	104	10 ^m	Inner cavity up to 19 au
PDS 66	K1Ve	86	17 ⁿ	Inner cavity up to 15 au

^a [Meeus et al. \(2012\)](#)

^b [Grady et al. \(2009\)](#)

^c [Mendigutía et al. \(2014\)](#)

^d [Fairlamb et al. \(2015\)](#)

^e [Ducourant et al. \(2014\)](#)

^f [Pecaut et al. \(2012\)](#); [Song et al. \(2012\)](#)

^g [D’Orazi et al. \(2019\)](#)

^h [Grady et al. \(2007\)](#)

ⁱ [Andrews et al. \(2009\)](#)

^j [van den Ancker et al. \(1998\)](#); [Lagage et al. \(2006\)](#); [van der Marel et al. \(2019\)](#)

^k [Merín et al. \(2004\)](#)

^l [Furlan et al. \(2008\)](#)

^m [Collins et al. \(2009\)](#)

ⁿ [Mamajek et al. \(2002\)](#)

with a 41×41 actuators wavefront control, pupil stabilization, and differential tip-tilt control ([Petit et al. 2014](#)). The instrument has three science subsystems: the infrared dual-band imager and spectrograph (IRDIS; [Dohlen et al. 2008](#)), an integral field spectrograph (IFS; [Claudi et al. 2008](#)), and the Zimpol rapid-switching imaging polarimeter (ZIMPOL; [Thalmann et al. 2008](#); [Schmid et al. 2018](#)). The latter, which is the only subsystem in visible light, has been used for the survey. The observing strategy was to take simultaneous images in the H α narrow band filter (N_Ha; $\lambda_c = 656.9$ nm, $\Delta\lambda = 1$ nm) and in H α continuum (Cont_Ha; $\lambda_c = 644.9$ nm, $\Delta\lambda = 4.1$ nm). We refer the reader to [Schmid et al. \(2018\)](#) for more details about the filters. All the observations were taken in pupil stabilized mode in order to take advantage of the speckles suppression technique of the angular differential imaging (ADI; [Marois et al. 2006](#)).

The observations (ESO programs 099.C-0453, 0100.C-0193, 0101.C-0461, 0102.C-0138, PI: Zurlo) were carried out in service mode, with the exception of the target DoAr 44 for which visitor mode was required during the last four ESO observing periods. To complete the sample for all the TDs that are closer than 200 pc and observable with SPHERE, we included the objects MWC 758, HD 135344B, and HD 142527 (programs 096.C-0267, PI: Huelamo, 096.C-0248, SPHERE GTO). The observations and analysis of the dataset of MWC 758 are presented in [Huélamo et al. \(2018\)](#). For this object, the broad band H α filter (B_Ha; $\lambda_c = 655.6$ nm, $\Delta\lambda = 3.35$ nm) was used. This same dataset, together with the datasets of the objects HD 135344B and HD 142527 are analysed in [Cugno et al.](#)

(2019). The different observing dates for each target, together with the total field of view rotation and the mean value of the seeing, are listed in Table 2. In general, the conditions were stable and the seeing was below $0.8''$. The total execution time per target was in between 1h and 1h30min.

3. Data reduction

The raw data were preprocessed using the ZIMPOL pipeline, an *IDL* routine developed at ETH Zurich. The pipeline produces bias-subtracted, flat-fielded, remapped images for each of the two filters. We refer the reader to [Cugno et al. \(2019\)](#), for further details. We used a python routine to recenter the images, with a Gaussian two-dimensional fitting and to create two different data cubes, one for the H α filter and one for the continuum. The python package *VIP* ([Gomez Gonzalez et al. 2017](#)) is used in this analysis. To perform the spectral differential imaging (SDI; [Lafrenière et al. 2007](#)) technique each image in the continuum filter was subtracted to the H α filter after being rescaled and normalized for the central point spread function (PSF).

More specifically, we first rescaled the continuum images. Additionally, in order to normalize the two PSFs, we used a minimum χ -square method, which minimizes the standard deviation inside a circle centered in the center of the image and with a radius of $5 \times \text{FWHM}$, after the subtraction of the two images. In this way, we are able to take the center of the PSF into account, in addition to its wings and the bright central speckles.

Table 2: Summary table of the observations of the survey.

Name	V mag	Obs date	DIT ^a xNDIT ^b	Rot (deg)	Seeing (")	Airmass
MWC 758*	8.3	30/12/2015	60x10	58	1.3	1.6
HD 135344 B*	8.7	31/03/2016	50x15	72	0.6	1.0
HD 142527*	8.3	31/03/2016	30x10	49	0.7	1.0
HD 100546	6.3	24/03/2016	120x5	57	2.8	1.5
		16/03/2019	9x20	27	0.8	1.4
HD 98800 B	10.1	08/01/2017	11x10	1	0.4	1.0
		12/01/2017	11x10	1	0.6	1.0
AK Sco	9.2	20/05/2017	40x4	39	0.5	1.0
V4046 Sgr AB	10.7	20/05/2017	60x4	99	0.5	1.0
		14/07/2017	15x5	39	0.6	1.0
HD 169142	8	28/05/2017	8x5	125	0.8	1.0
		17/05/2018	9x17	84	0.4	1.0
DoAr 44	11.7	29/06/2017	60x2	3	0.9	1.0
HD 97048	8.5	06/02/2018	7x15	23	0.3	1.7
		22/02/2019	11x20	23	0.7	1.7
HD 141569 A	7.1	22/03/2018	8x18	29	0.7	1.0
		17/05/2018	11x20	43	0.5	1.0
UX Tau A	11.1	26/11/2018	110x2	24	0.4	1.4
HD 100453	7.8	20/01/2019	11x20	36	0.5	1.2
PDS 66	10.4	22/03/2019	24x10	34	0.5	1.5

^a Detector Integration Time

^b Number of frames per dithering position

We then performed a principal component analysis (PCA) reduction to apply the ADI method with a different number of components, depending on the total number of frames of each observation. In most of the cases, a frame selection rejecting low-quality frames (with a maximum of the 25% of the total number) was applied. We refer to angular spectral differential imaging (ASDI) reduction as the combination of angular and spectral differential imaging. To align the images, we applied a true north correction of 134 ± 0.5 deg as in [Cugno et al. \(2019\)](#).

A couple of examples of the final ASDI PCA image are shown in [Fig. 1](#) for the object HD 142527 B and [Fig. 2](#) for the quadruple system around HD 98800. The two stellar companions of the spectroscopic binary were resolved at these wavelengths for the first time.

4. Analysis and results

No significant detection of point sources has been recovered from the data reduction, apart from the already known stellar companion of HD 142527, which is presented in [Sec. 4.1](#), and the two stellar companions of HD 98800 Ba, in [Sec. 4.2](#). On the other hand, the contrast curves produced reflect the good conditions and exquisite performance of the instrument. We refer the reader to [Zurlo et al. \(2014, 2016\)](#) for a detailed explanation of how we calculated the contrast curves.

In [Figure 3](#), we present the contrast curves for the target AK Sco in addition to V4046Sgr A ([Fig. 4](#)), HD 169142 ([Fig. 5](#)), HD 97048 ([Fig. 6](#)), HD 100546 ([Fig. 7](#)), HD 142527 ([Fig. 8](#)), HD 141569A ([Fig. 9](#)), HD 135344B ([Fig. 10](#)), UX TauA ([Fig. 11](#)), PDS 66 ([Fig. 12](#)), and HD 100453 ([Fig. 13](#)). In the case of multiple datasets for the same object we selected and show here the best one. The reduction was performed for all the datasets. In general, we could reach a very deep contrast of ~ 12 mag at $0''.2$ separation from the host star.

Similarly to [Cugno et al. \(2019\)](#), in order to estimate the stellar flux in the continuum filter, we calculated the median of the

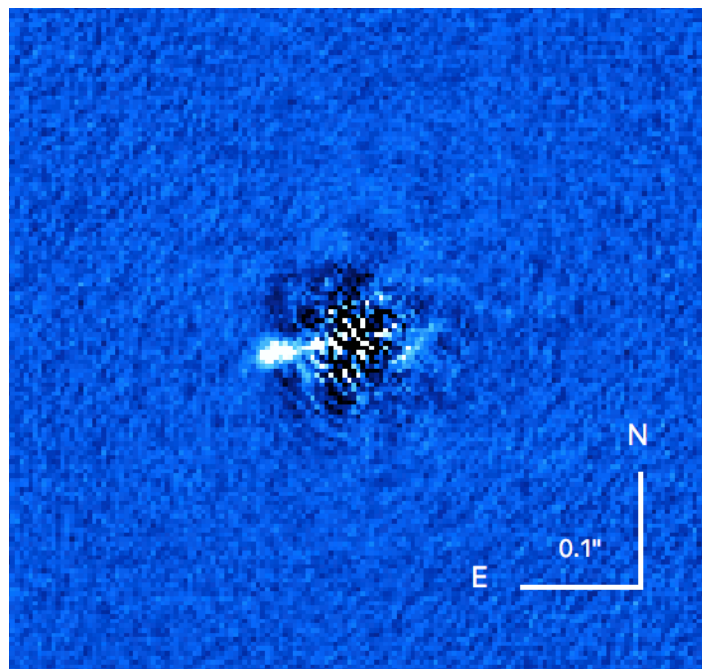


[Fig. 1](#): ASDI image of the system HD 142527. The stellar accretion companion is visible in the East. The image shows the very close vicinity of the stellar companion.

count rate in an aperture of radius 1.5 arcsec and applied it in [Eq. 4](#) from [Schmid et al. \(2017\)](#) after subtracting the background calculated in a ring at $r = 1''$ (see [Musso Barucci et al. 2019](#)). The filter zero point was also taken from [Schmid et al. \(2017\)](#). The calculated flux density was multiplied by the continuum filter effective width of 41.1 Angstrom (see [Schmid et al. 2018](#)) in order to obtain the stellar flux. Subsequently, for each object, the

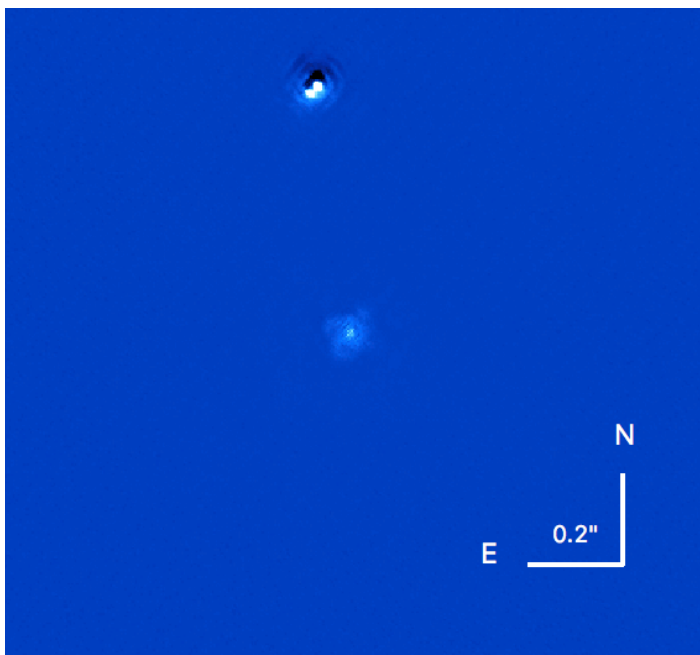


Fig. 2: ASDI image of the system HD 98800 BaBb. The system is a quadruple: two spectroscopic binaries at the center of the detector and two stellar companions (one accreting) are visible in the north, which are resolved for the first time in the visible.

contrast at each separation, which was calculated with respect to the PSF in the continuum images, was applied and the flux limit was directly calculated and converted into H α luminosity. The relationship between H α luminosity and accretion luminosity, as presented in Rigliaco et al. (2012), was used to obtain the upper limit for the accretion luminosity (as in Cugno et al. 2019). From simulations these formulas were also confirmed for planets (Thanathibodee et al. 2019). In Fig. 14, we show the apparent flux limit for all the targets and the accretion luminosity in Fig. 15. In Fig. 16, we show the mass accretion rate limits if we assume a planet of fixed mass $5 M_{\text{Jup}}$ and $1.47 R_{\text{Jup}}$ (for the mean age of our sample), and by exploiting the AMES-COND evolutionary models (Allard et al. 2001) as in Cugno et al. (2019). The same Eq. 4 of Cugno et al. (2019) was applied for the calculation.

In summary:

- For all the targets of our sample, on average we reach H α line flux sensitivities, H α line luminosities and accretion luminosity upper limits of 2×10^{-15} erg/s/cm 2 , $5 \times 10^{-7} L_{\odot}$, and $10^{-6} L_{\odot}$ respectively, beyond 0''.2.
- We reach an average mass accretion rate sensitivity of $10^{-9} M_{\text{Jup}}/\text{yr}$ beyond 0''.2 for planets of $5 M_{\text{Jup}}$.
- The best sensitivities were obtained for AK Sco, HD 142527, and PDS 66 targets.
- The worst sensitivity was obtained for DoAr 44 because of the faintness of the central star ($V=12.8$), which is located at the limit of the adaptive optics (AO) system.
- In half of the cases, we reached sufficient sensitivity to re-detect PDS 70 b.

4.1. HD 142527

HD 142527 is a Herbig Ae/Be star that harbors a TD (e.g., Canovas et al. 2013; Boehler et al. 2017; Avenhaus et al. 2017)

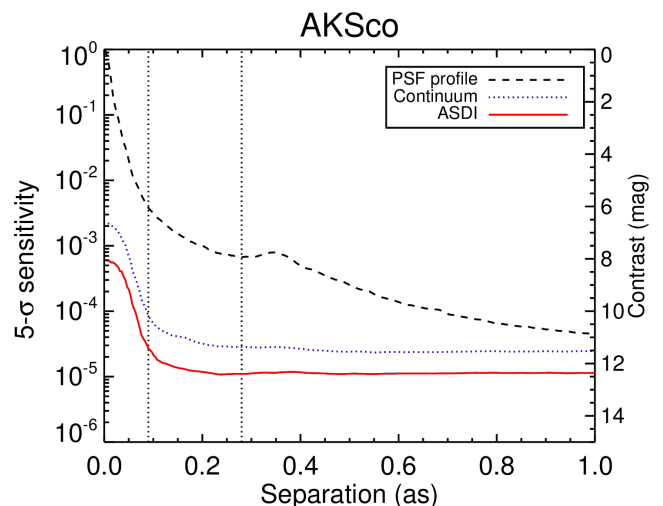


Fig. 3: Contrast plot for the object AK Sco. In a black solid line, the profile of the PSF is shown, blue represents the H α continuum filter after being processed with PCA and ADI, and red is the ASDI contrast. The vertical dotted lines represent the extension of the spirals (Janson et al. 2016).

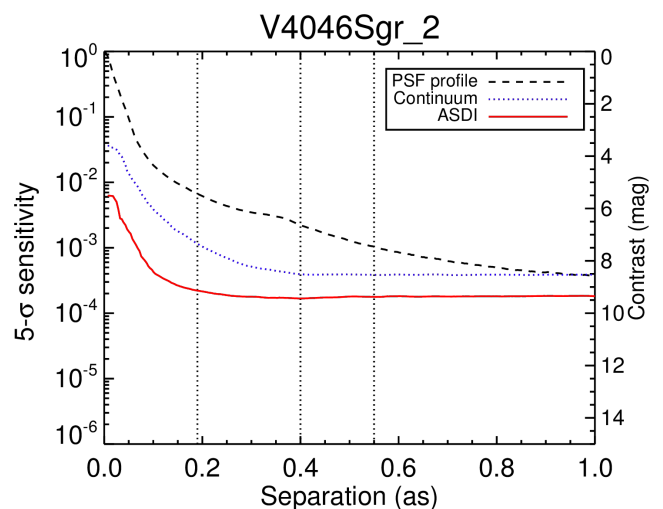


Fig. 4: Same as Fig. 3, but for the object V4046 Sgr. The vertical dotted lines represent the locations of the rings detected by Rapson et al. (2015) and Avenhaus et al. (2018).

and an M star accreting companion (Biller et al. 2012; Close et al. 2014; Christiaens et al. 2018; Claudi et al. 2019). Price et al. (2018) suggest that the shape of the disk has been carved by the interaction with the binary. Claudi et al. (2019) retrieved the orbit for the companion using all the astrometric data available to date, they found a period of $P = 35\text{--}137$ yr; an inclination of $i = 121\text{--}130$ deg, and two families of values for the eccentricity: 0.2–0.45 and 0.45–0.7. In our data, the astrometry for the stellar companion is as follows: separation of 63.0 ± 1.5 mas and PA 96.4 ± 1 deg, which is consistent with the previous results from Cugno et al. (2019) and Claudi et al. (2019).

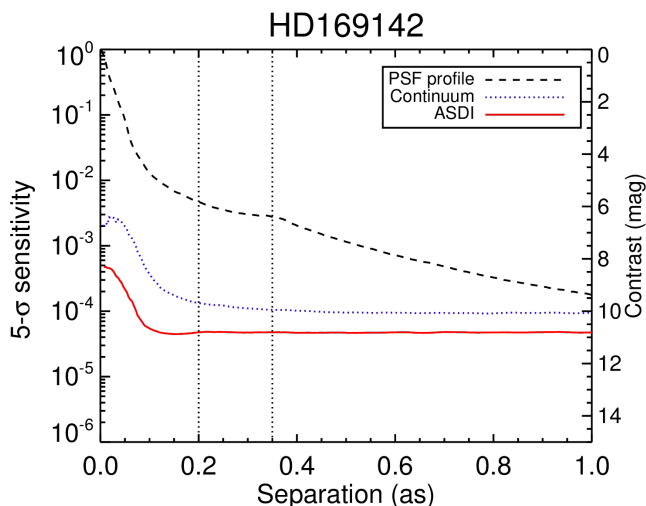


Fig. 5: Same as Fig. 3, but for the object HD 169142. The vertical dotted lines represent the location of the gaps detected by [Honda et al. \(2012\)](#) and [Pohl et al. \(2017\)](#).

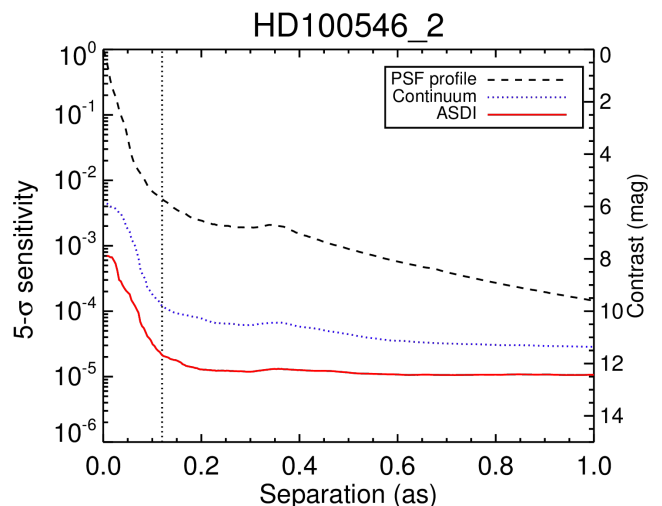


Fig. 7: Same as Fig. 3, but for the object HD 100546. The dotted vertical line is located at the position of the inner gap ([Quanz et al. 2015](#)).

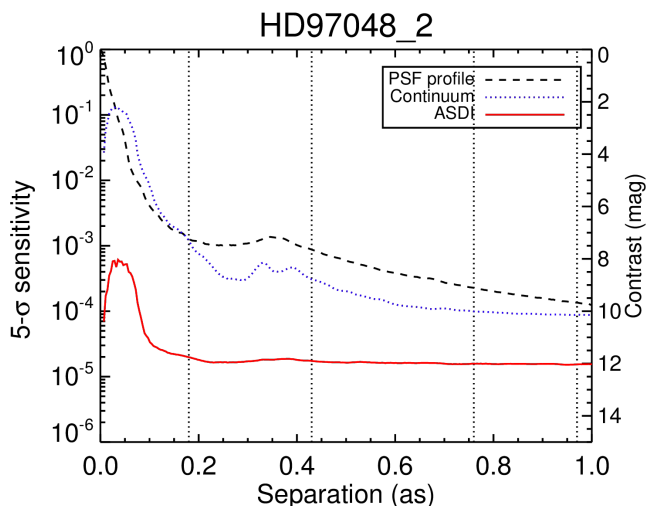


Fig. 6: Same as Fig. 3, but for the object HD 97048. The vertical dotted lines represent the location of the gaps detected by [Ginski et al. \(2016\)](#).

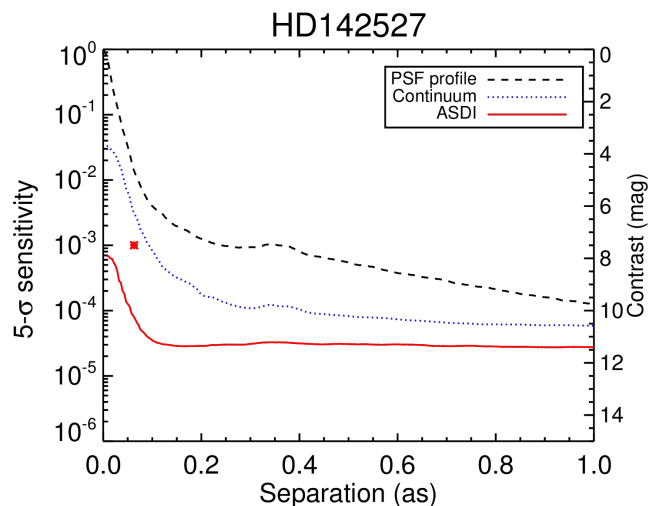


Fig. 8: Same as Fig. 3, but for the object HD 142527. The red point represents the detected stellar companion.

4.2. HD 98800

HD 98800 is a quadruple system at a distance of 47 pc ([van Leeuwen 2007](#)), which is composed of the following two binaries: HD 98800 BaBb, at a projected separation of $0''.8$ from the spectroscopic binaries, and HD 98800 AaAb, which has a separation of ~ 1 au ([Boden et al. 2005](#)). Around the B component, [Furlan et al. \(2007\)](#) found a transition disk composed of an optically thin component with an inner radius of 2 au, then a gap, and an optically thick component with a radius of 5.9 au. The presence of the gap might be explained by the carving of a planet. [Kennedy et al. \(2019\)](#) show ALMA results of the system, which present a very compact dust ring that is 2-au wide at a radius of 3.5 au. Because of a misunderstanding regarding the finding chart, the observations were carried out with the A component in the center of the image, and they will be performed again. The

two stellar companions (HD 98800 BaBb) of the spectroscopic binary were resolved in the visible for the first time.

The two stellar components, which were resolved in the ZIMPOL images, have a separation with respect to the A star of 495.8 ± 1.5 mas and a position angle of 9.0 ± 1.0 deg, and a separation of 507.5 ± 1.5 mas, position angle of 7.5 ± 1.0 deg. They are separated by 17.7 mas. The brightest component (west component) has an $H\alpha$ flux of 6.5×10^{-16} L_{\odot} , an $H\alpha$ luminosity of 4.6×10^{-8} L_{\odot} , and an accretion luminosity of 1.1×10^{-8} L_{\odot} , while the faintest is not accreting.

5. Discussion and conclusions

We conducted a survey of nearby (< 200 pc) TDs seen in the $H\alpha$ filter. The purpose was to look for accreting protoplanets in all the disks that present peculiar features that can be induced by

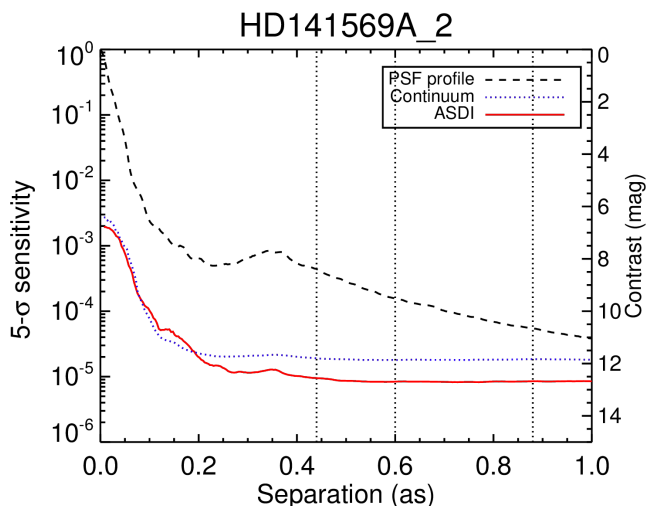


Fig. 9: Same as Fig. 3, but for the object HD 141569A. The vertical dotted lines represent the location of the ringlets detected by Perrot et al. (2016).

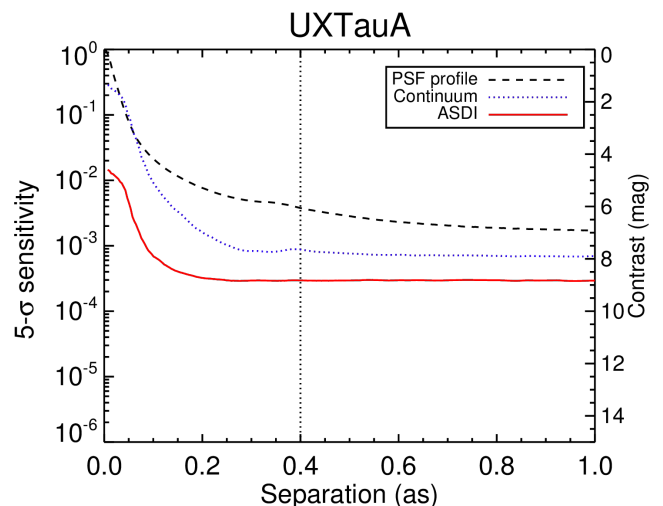


Fig. 11: Same as Fig. 3, but for the object UX Tau A. The vertical dotted line represents the location of the gap (Espaillat et al. 2007).

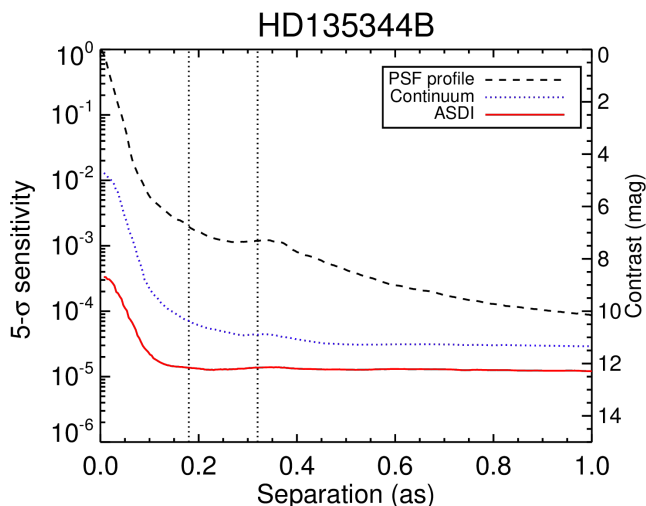


Fig. 10: Same as Fig. 3, but for the object HD 135344B. The two dotted lines represent the extension of the spiral arms detected by van der Marel et al. (2016) and Hammer et al. (2019).

the presence of companions. The survey, which was conducted with SPHERE/ZIMPOL, made use of the ASDI technique between the $H\alpha$ narrow filter and the adjacent continuum. Eleven targets were observed in excellent conditions (seeing $< 0''.8$) and the other three targets were added to the analysis for completeness. We did not detect any previously unknown companions, although the two components of HD 99880 BaBb were resolved for the first time in the visible.

The contrast curves that we obtained for the targets of the survey reflect the exquisite performance of the instrument, and they give strong constraints on the presence of accreting companions around the selected stars. If we compare our detection limits with the predictions from the population synthesis of Mordasini et al. (2017), while also assuming complete cold accretion, we expect to be unable to spot low mass ($< 1 M_{\text{Jup}}$) medium

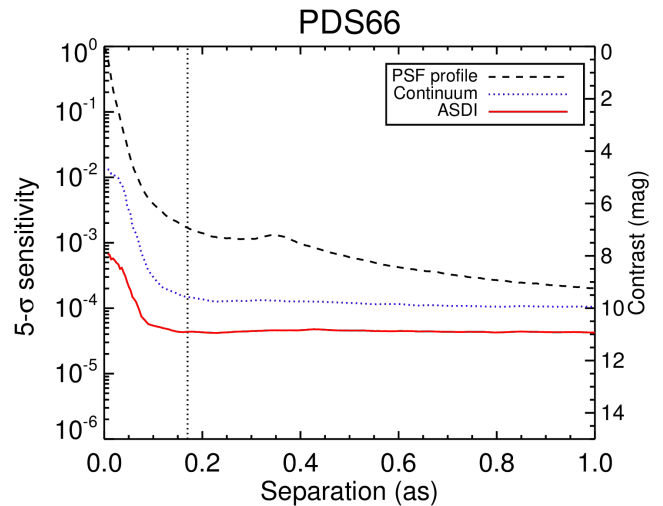


Fig. 12: Same as Fig. 3, but for the object PDS 66. The vertical dotted line represents the location of the inner cavity (Gräfe & Wolf 2013; Wolff et al. 2016).

accreting ($\dot{M} = 10^{-5\pm 1} M_{\text{Jup}} \text{ yr}^{-1}$) planets or high mass ($1-15 M_{\text{Jup}}$) that are not heavily accreting ($\dot{M} < 10^{-5.5} M_{\text{Jup}} \text{ yr}^{-1}$).

The detection limits that we found can help us to investigate some properties of the putative protoplanets; the mass M_p , the planet radius R_p , and the planetary accretion rates \dot{M} . Assuming the accretion disk paradigm, it has been theorized that the $H\alpha$ luminosity, which is produced by shocks at some distance R_s (magnetospheric radius), can be approximated by

$$L_{H\alpha} = 4\pi R_s^2 \pi B_\nu(T) \nu_{H\alpha} v_s / c, \quad (1)$$

where $\nu_{H\alpha}$ is the $H\alpha$ line frequency, v_s the free-fall velocity of the accreting gas, c the speed of light, $B_\nu(T)$ the Planck function, and T the temperature of the shock, which is generated by the gravitational conversion between gas accretion to accretion shock luminosity, that is, $L_{\text{shock}} = \zeta GM_p \dot{M} / R_p$, and where

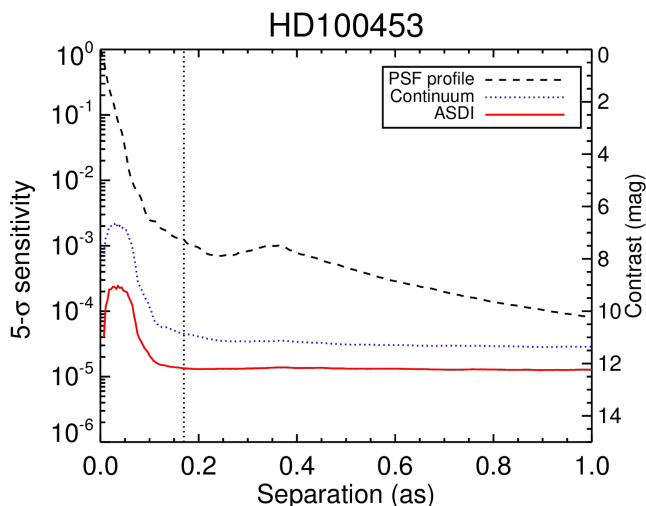


Fig. 13: Same as Fig. 3, but for the object HD 100453. The vertical dotted line represents the inner part of the spirals detected by Dong & Fung (2017).

$\zeta = 1 - R_p/R_T$, where R_T is the truncation radius (Zhu 2015a). We used $R_T \sim 5R_p$ for the truncation radius, as in Cugno et al. (2019).

The shock temperature should be high enough to partially ionize the Hydrogen to be compatible with $H\alpha$ emission, therefore $T \sim 10^4 - 10^8$ K (Aoyama et al. 2018). The value of v_s is crudely known, but it was estimated to be in the range $\sim 50 - 100$ km s^{-1} for accreting circumplanetary disks (Zhu 2015a; Aoyama & Ikoma 2019). Also, v_s can be approximated by

$$v_s = (2GM_p/R_p)^{1/2}\zeta^{1/2}, \quad (2)$$

where R_p and M_p are the radius and mass of the planet, respectively.

Our detection limits give an upper boundary $H\alpha$ luminosity of $L_{H\alpha} = 5 \times 10^{-7} L_\odot$. In assuming that the magnetospheric accretion shock occurs at the planet surface, we constrained the maximum planetary-mass able to produce such emission by equating this upper-limit $L_{H\alpha}$ to Eq. (1). For instance, if we assume a shock temperature of $T = 10^4$ K and $v_s = 50, 100$ km s^{-1} , we obtain from Eq. (1) (assuming $R_T = 5R_p$); $R_p = 1.3, 0.9 R_{Jup}$, respectively. Using the resulting R_p , we derived the following planetary masses from Eq. (2); $1.1, 3.3 M_{Jup}$, respectively, making the second example with high free-fall velocity less realistic.

It has yet to be determined if some of the nondetections are due to the intrinsic variability of protoplanets, which can be highly variable over time, changing their luminosity on short timescales on the order of hours. That could be a possible explanation for the nondetection of these kinds of objects, despite the very high sensitivity that we can reach with the current instrumentation. If this is the case, in the future, multiepoch observations are necessary to unveil the nature of accreting protoplanets in transition disks.

Another possible explanation for the nondetections could be that accreting planets are located within ~ 200 mas from the host star, where our observation are not sensitive enough due to the bright central speckles. Also, one has to consider that the assumptions that we are making in order to derive accretion lumi-

nosities from line luminosities may be inappropriate. For example, the estimate of the PDS 70 b accretion rate, using the different accretion luminosity estimate by Aoyama & Ikoma (2019), was much higher than the one presented in Wagner et al. (2018) for the same line luminosity. This could mean that a given accretion rate would correspond to a lower line luminosity if more realistic conversions are applied.

Acknowledgements. We thank the anonymous referee for the constructive comments that improved the manuscript. A.Z. acknowledges support from the CONICYT + PAI/ Convocatoria nacional subvención a la instalación en la academia, convocatoria 2017 + Folio PAI77170087. G.C. thanks the Swiss National Foundation for the financial support under the grant number 200021_169131. M.M. acknowledges financial support from the Chinese Academy of Sciences (CAS) through a CAS-CONICYT Postdoctoral Fellowship administered by the CAS South America Center for Astronomy (CASSACA) in Santiago, Chile, and support from Iniciativa Científica Milenio via the Núcleo Milenio de Formación Planetaria. N.H. has been partially funded by the Spanish State Research Agency (AEI) Project No. ESP2017-87676-C5-1-R and No. MDM-2017-0737 Unidad de Excelencia *María de Maeztu* - Centro de Astrobiología (INTA-CSIC).

References

- Allard, F., Hauschildt, P. H., Alexander, D. R., Tamanai, A., & Schweitzer, A. 2001, *ApJ*, 556, 357
- Andrews, S. M., Wilner, D. J., Hughes, A. M., Qi, C., & Dullemond, C. P. 2009, *ApJ*, 700, 1502
- Aoyama, Y. & Ikoma, M. 2019, *ApJ*, 885, L29
- Aoyama, Y., Ikoma, M., & Tanigawa, T. 2018, *ApJ*, 866, 84
- Avenhaus, H., Quanz, S. P., Garufi, A., et al. 2018, *ApJ*, 863, 44
- Avenhaus, H., Quanz, S. P., Schmid, H. M., et al. 2017, *AJ*, 154, 33
- Beuzit, J. L., Vigan, A., Mouillet, D., et al. 2019, *A&A*, 631, A155
- Billier, B., Lacour, S., Juhász, A., et al. 2012, *ApJ*, 753, L38
- Billier, B. A., Males, J., Rodigas, T., et al. 2014, *ApJ*, 792, L22
- Boden, A. F., Sargent, A. I., Akeson, R. L., et al. 2005, *ApJ*, 635, 442
- Boehler, Y., Weaver, E., Isella, A., et al. 2017, *ApJ*, 840, 60
- Canovas, H., Ménard, F., Hales, A., et al. 2013, *A&A*, 556, A123
- Casassus, S., Avenhaus, H., Pérez, S., et al. 2018, *MNRAS*, 477, 5104
- Christiaens, V., Cantalloube, F., Casassus, S., et al. 2019, *ApJ*, 877, L33
- Christiaens, V., Casassus, S., Absil, O., et al. 2018, *A&A*, 617, A37
- Claudi, R., Maire, A. L., Mesa, D., et al. 2019, *A&A*, 622, A96
- Claudi, R. U., Turatto, M., Gratton, R. G., et al. 2008, in Society of Photo-Optical Instrumentation Engineers (SPIE) Conference Series, Vol. 7014, Society of Photo-Optical Instrumentation Engineers (SPIE) Conference Series
- Close, L. M., Follette, K. B., Males, J. R., et al. 2014, *ApJ*, 781, L30
- Collins, K. A., Grady, C. A., Hamaguchi, K., et al. 2009, *ApJ*, 697, 557
- Cugno, G., Quanz, S. P., Hunziker, S., et al. 2019, *A&A*, 622, A156
- Currie, T., Cloutier, R., Brittain, S., et al. 2015, *ApJ*, 814, L27
- Currie, T., Marois, C., Cieza, L., et al. 2019, *ApJ*, 877, L3
- Dodson-Robinson, S. E. & Salyk, C. 2011, *ApJ*, 738, 131
- Dohlen, K., Langlois, M., Saisse, M., et al. 2008, in Society of Photo-Optical Instrumentation Engineers (SPIE) Conference Series, Vol. 7014, Society of Photo-Optical Instrumentation Engineers (SPIE) Conference Series
- Dong, R. & Fung, J. 2017, *ApJ*, 835, 38
- Dong, R., Fung, J., & Chiang, E. 2016a, *ApJ*, 826, 75
- Dong, R., Zhu, Z., Fung, J., et al. 2016b, *ApJ*, 816, L12
- Dong, R., Zhu, Z., Rafikov, R. R., & Stone, J. M. 2015, *ApJ*, 809, L5
- D’Orazi, V., Gratton, R., Desidera, S., et al. 2019, *Nature Astronomy*, 3, 167
- Ducourant, C., Teixeira, R., Galli, P. A. B., et al. 2014, *A&A*, 563, A121
- Españillat, C., Calvet, N., D’Alessio, P., et al. 2007, *ApJ*, 670, L135
- Fairlamb, J. R., Oudmaijer, R. D., Mendigutía, I., Ilee, J. D., & van den Ancker, M. E. 2015, *MNRAS*, 453, 976
- Fortney, J. J., Lodders, K., Marley, M. S., & Freedman, R. S. 2008, *ApJ*, 678, 1419
- Furlan, E., McClure, M., Calvet, N., et al. 2008, *ApJS*, 176, 184
- Furlan, E., Sargent, B., Calvet, N., et al. 2007, *ApJ*, 664, 1176
- Gaia Collaboration. 2018, *VizieR Online Data Catalog*, I/345
- Ginski, C., Stolker, T., Pinilla, P., et al. 2016, *A&A*, 595, A112
- Gomez Gonzalez, C. A., Wertz, O., Absil, O., et al. 2017, *AJ*, 154, 7
- Grady, C. A., Schneider, G., Hamaguchi, K., et al. 2007, *ApJ*, 665, 1391
- Grady, C. A., Schneider, G., Sitko, M. L., et al. 2009, *ApJ*, 699, 1822
- Gräfe, C. & Wolf, S. 2013, *A&A*, 552, A88
- Gressel, O., Nelson, R. P., Turner, N. J., & Ziegler, U. 2013, *ApJ*, 779, 59
- Haffert, S. Y., Bohn, A. J., de Boer, J., et al. 2019, *Nature Astronomy*, 3, 749
- Hammer, M., Pinilla, P., Kratter, K. M., & Lin, M.-K. 2019, *MNRAS*, 482, 3609
- Honda, M., Maaskant, K., Okamoto, Y. K., et al. 2012, *ApJ*, 752, 143
- Huélamo, N., Chauvin, G., Schmid, H. M., et al. 2018, *A&A*, 613, L5

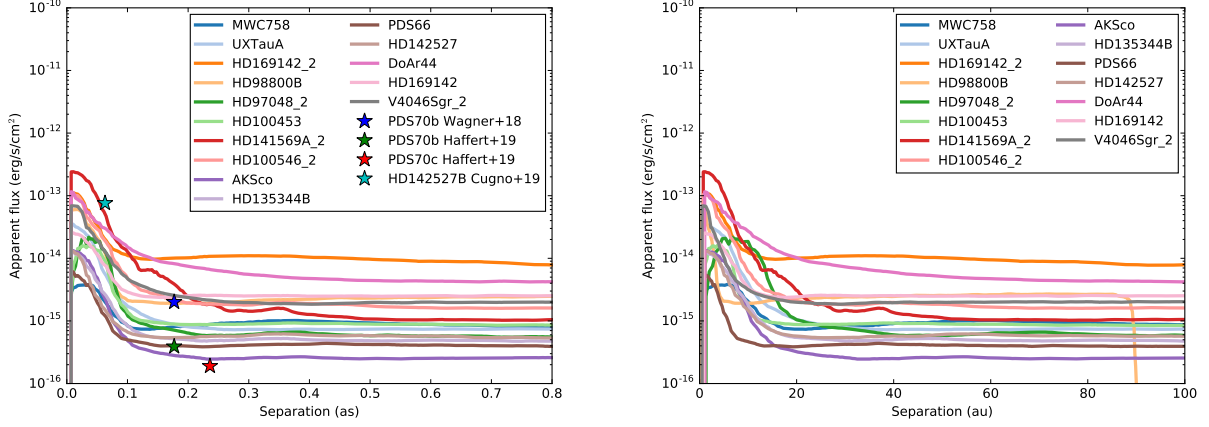


Fig. 14: Apparent $H\alpha$ line flux limits for all the targets of the sample versus angular separation (left) and physical separation (right). The differences between our predictions and other cases from the literature are primarily related to the methods used to extrapolate the accretion luminosity from the $H\alpha$ line flux; as with SPHERE, the line width cannot be measured.

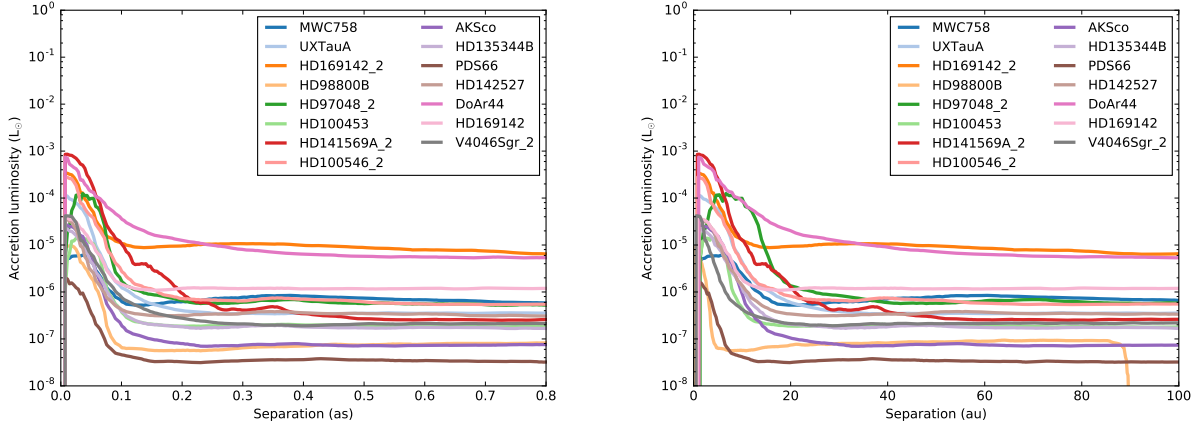


Fig. 15: Accretion luminosity limits for all the targets of the sample versus angular separation (left) and physical separation (right).

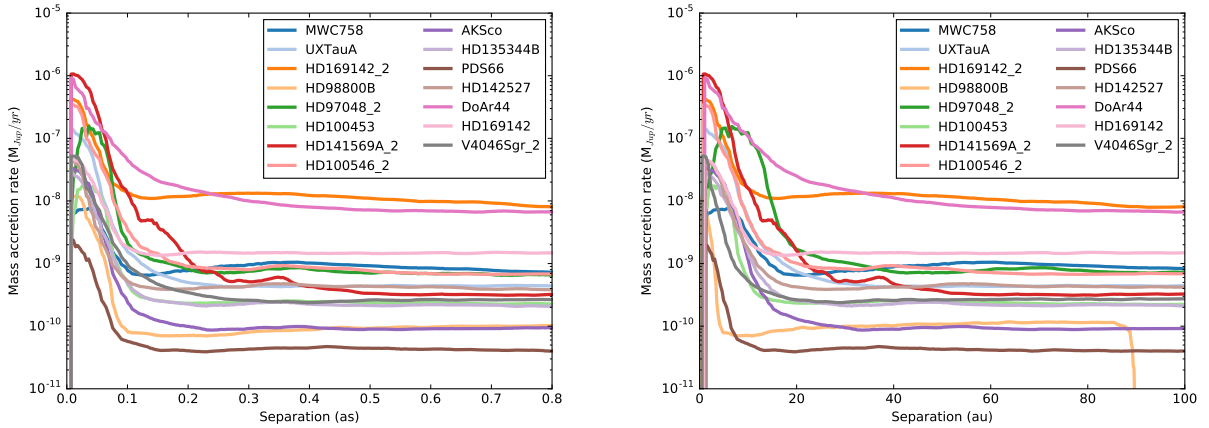


Fig. 16: Mass accretion rate limits (for a $5 M_{\text{Jup}}$ mass planet) for all the targets of the sample versus angular separation (left) and physical separation (right).

- Janson, M., Thalmann, C., Boccaletti, A., et al. 2016, *ApJ*, 816, L1
- Kama, M., Folsom, C. P., & Pinilla, P. 2015, *A&A*, 582, L10
- Kennedy, G. M., Matrà, L., Facchini, S., et al. 2019, *Nature Astronomy*, 3, 278
- Keppler, M., Benisty, M., Müller, A., et al. 2018, *A&A*, 617, A44
- Lafrenière, D., Marois, C., Doyon, R., Nadeau, D., & Artigau, É. 2007, *ApJ*, 660, 770
- Lagage, P.-O., Doucet, C., Pantin, E., et al. 2006, *Science*, 314, 621
- Ligi, R., Vigan, A., Gratton, R., et al. 2018, *MNRAS*, 473, 1774
- Macintosh, B., Graham, J., Palmer, D., et al. 2006, in *Society of Photo-Optical Instrumentation Engineers (SPIE) Conference Series*, Vol. 6272, 62720L
- Mamajek, E. E., Meyer, M. R., & Liebert, J. 2002, *AJ*, 124, 1670
- Marois, C., Lafrenière, D., Doyon, R., Macintosh, B., & Nadeau, D. 2006, *ApJ*, 641, 556
- Meeus, G., Montesinos, B., Mendigutía, I., et al. 2012, *A&A*, 544, A78
- Mendigutía, I., Fairlamb, J., Montesinos, B., et al. 2014, *ApJ*, 790, 21
- Mendigutía, I., Oudmaijer, R. D., Garufi, A., et al. 2017, *A&A*, 608, A104
- Mendigutía, I., Oudmaijer, R. D., Schneider, P. C., et al. 2018, *A&A*, 618, L9
- Merín, B., Montesinos, B., Eiroa, C., et al. 2004, *A&A*, 419, 301
- Mesa, D., Keppler, M., Cantalloube, F., et al. 2019, *A&A*, 632, A25
- Miki, S. 1982, *Progress of Theoretical Physics*, 67, 1053
- Montesinos, M., Cuadra, J., Perez, S., Baruteau, C., & Casassus, S. 2015, *ApJ*, 806, 253
- Morbidelli, A., Szulágyi, J., Crida, A., et al. 2014, *Icarus*, 232, 266
- Mordasini, C., Marleau, G. D., & Mollière, P. 2017, *A&A*, 608, A72
- Müller, A., Keppler, M., Henning, T., et al. 2018, *A&A*, 617, L2
- Musso Barucci, A., Cugno, G., Launhardt, R., et al. 2019, *A&A*, 631, A84
- Pecaut, M. J., Mamajek, E. E., & Bubar, E. J. 2012, *ApJ*, 746, 154
- Perez, S., Dunhill, A., Casassus, S., et al. 2015, *ApJ*, 811, L5
- Perrot, C., Boccaletti, A., Pantin, E., et al. 2016, *A&A*, 590, L7
- Petit, C., Sauvage, J.-F., Fusco, T., et al. 2014, in *Proc. SPIE*, Vol. 9148, *Adaptive Optics Systems IV*, 91480O
- Pinte, C., van der Plas, G., Ménard, F., et al. 2019, *Nature Astronomy*, 419
- Pohl, A., Benisty, M., Pinilla, P., et al. 2017, *ApJ*, 850, 52
- Price, D. J., Cuello, N., Pinte, C., et al. 2018, *MNRAS*, 477, 1270
- Quanz, S. P., Amara, A., Meyer, M. R., et al. 2015, *ApJ*, 807, 64
- Rameau, J., Follette, K. B., Pueyo, L., et al. 2017, *AJ*, 153, 244
- Rapson, V. A., Kastner, J. H., Andrews, S. M., et al. 2015, *ApJ*, 803, L10
- Reggiani, M., Christiaens, V., Absil, O., et al. 2018, *A&A*, 611, A74
- Reggiani, M., Quanz, S. P., Meyer, M. R., et al. 2014, *ApJ*, 792, L23
- Rigliaco, E., Natta, A., Testi, L., et al. 2012, *A&A*, 548, A56
- Sallum, S., Follette, K. B., Eisner, J. A., et al. 2015, *Nature*, 527, 342
- Schmid, H. M., Bazzon, A., Milli, J., et al. 2017, *Astronomy and Astrophysics*, 602, A53
- Schmid, H. M., Bazzon, A., Roelfsema, R., et al. 2018, *A&A*, 619, A9
- Sissa, E., Gratton, R., Garufi, A., et al. 2018, *A&A*, 619, A160
- Song, I., Zuckerman, B., & Bessell, M. S. 2012, *AJ*, 144, 8
- Spiegel, D. S. & Burrows, A. 2012, *ApJ*, 745, 174
- Szulágyi, J., Morbidelli, A., Crida, A., & Masset, F. 2014, *ApJ*, 782, 65
- Tambovtseva, L. V., Grinin, V. P., & Weigelt, G. 2014, *A&A*, 562, A104
- Tanigawa, T., Ohtsuki, K., & Machida, M. N. 2012, *ApJ*, 747, 47
- Thalmann, C., Janson, M., Garufi, A., et al. 2016, *ApJ*, 828, L17
- Thalmann, C., Schmid, H. M., Boccaletti, A., et al. 2008, in *Society of Photo-Optical Instrumentation Engineers (SPIE) Conference Series*, Vol. 7014, *Society of Photo-Optical Instrumentation Engineers (SPIE) Conference Series*
- Thanathibodee, T., Calvet, N., Bae, J., Muzerolle, J., & Hernández, R. F. 2019, *ApJ*, 885, 94
- van den Ancker, M. E., de Winter, D., & Tjin A Djie, H. R. E. 1998, *A&A*, 330, 145
- van der Marel, N., Cazzoletti, P., Pinilla, P., & Garufi, A. 2016, *ApJ*, 832, 178
- van der Marel, N., Dong, R., di Francesco, J., Williams, J. P., & Tobin, J. 2019, *ApJ*, 872, 112
- van Leeuwen, F. 2007, *A&A*, 474, 653
- Wagner, K., Follette, K. B., Close, L. M., et al. 2018, *ApJ*, 863, L8
- Wolff, S. G., Perrin, M., Millar-Blanchaer, M. A., et al. 2016, *ApJ*, 818, L15
- Zhu, Z. 2015a, *ApJ*, 799, 16
- Zhu, Z. 2015b, *Nature*, 527, 310
- Zurlo, A., Vigan, A., Galicher, R., et al. 2016, *A&A*, 587, A57
- Zurlo, A., Vigan, A., Mesa, D., et al. 2014, *A&A*, 572, A85